



Influence of anionic vacancies on the conductivity of $\text{La}_{0.33}\text{Si}_{6-x}\text{Al}_x\text{O}_{26-x/2}$ oxide conductors with an oxyapatite structure

A. Inoubli ^{a,b,*}, M. Kahlaoui ^a, I. Sobrados ^c, S. Chefi ^a, A. Madani ^a, J. Sanz ^c,
A. Ben Haj Amara ^b

^a Laboratoire de physique des Matériaux, Faculté des Sciences de Bizerte, Université de Carthage, Zarzouna 7021, Tunisia

^b Laboratoire de Physique des Matériaux Lamellaires et Nano-Matériaux Hybrides, Faculté des Sciences de Bizerte, Université de Carthage, Zarzouna 7021, Tunisia

^c Instituto de Ciencia de Materiales de Madrid (ICMM), Consejo Superior de Investigaciones Científicas (CSIC), Cantoblanco, 28049 Madrid, Spain

HIGHLIGHTS

- $\text{La}_{0.33}\text{Si}_{6-x}\text{Al}_x\text{O}_{26-x/2}$ oxyapatite is studied for applications in SOFCs.
- The conductivity for Al-doped oxyapatites increased with the Al content increase.
- The expansion of the La(1)–O(4) distance, facilitating the O^{2-} ion migration and thus enhancing the conduction.
- The ionic conductivity of $\text{La}_{0.33}\text{Si}_5\text{Al}_1\text{O}_{25.5}$ reaches $5 \times 10^{-3} \text{ S cm}^{-1}$ at 750°C .

ARTICLE INFO

Article history:

Received 23 May 2014

Received in revised form

17 July 2014

Accepted 21 July 2014

Available online 4 August 2014

Keywords:

Oxyapatites

Doped lanthanum silicate

Solid oxide fuel cells

Ionic conductivity

Impedance spectroscopy

Anionic vacancies

ABSTRACT

Al-doped oxyapatite-type lanthanum silicates $\text{La}_{0.33}\text{Si}_{6-x}\text{Al}_x\text{O}_{26-x/2}$ ($x = 0, 0.4, 0.8$ and 1) powders have been prepared by the solid state reaction at high temperature in order to determine the influence of anionic vacancies on the electrical properties of the material. The crystal structure and properties of $\text{La}_{0.33}\text{Si}_{6-x}\text{Al}_x\text{O}_{26-x/2}$ powders have been studied by X-ray diffraction (XRD) patterns, magic-angle spinning nuclear magnetic resonance (MAS-NMR) technique and complex impedance analysis. All the compounds of $\text{La}_{0.33}\text{Si}_{6-x}\text{Al}_x\text{O}_{26-x/2}$ oxyapatites doped with Al^{3+} consist of a hexagonal structure with a P63/m space group. Lanthanum silicates doped with trivalent Al^{3+} have a higher conductivity than those without trivalent Al^{3+} at the Si^{4+} site. The extra oxygen O(4) atoms in site 2a (0, 0, 0.25) occupy channels running through the structure that are responsible for the high oxygen ion conduction. However, Al substitution seems to produce oxygen vacancies and create another pathway for oxide ions. The expansion of the channels (La(1)–O(4) distance) leads to an increase in the conductivity. For the best sample ($x = 1$), the conductivity observed was $5 \times 10^{-3} \text{ S cm}^{-1}$ at 750°C .

© 2014 Elsevier B.V. All rights reserved.

1. Introduction

Oxyapatite lanthanum silicates have attracted great attention as candidates for intermediate temperature electrolytes of solid oxide fuel cells (SOFCs), due to their low operating temperature of less than $600\text{--}800^\circ\text{C}$, excellent long-term stability, a wide range of material selection and a relatively low processing cost [1–5].

The oxyapatite structure consists (Fig. 1) of isolated and covalent silicate tetrahedrons which form the “rigid” part of the structure [6,7]. The La(1) cations are located in a seven coordinate site (named 6h) and form a channel along the “c” axis. The La(2) cations are located in a nine coordinate site (named 4f) between each ionic plane of the structure. The O(4) (2a) anions are located in the channels formed by the La(1) cations and are responsible for the good ionic conductivity of this structure. The framework exhibits channels along the c-axis where oxide ions migrate to [8–10]. In the literature, the oxyapatite structure has usually been shown to have hexagonal symmetry, and to crystallize in the P63/m space group [6,11–13].

Doping cations with a relatively low valence for the Si site helps increase the conductivity of oxyapatite lanthanum silicates. For

* Corresponding author. Laboratoire de physique des Matériaux, Faculté des Sciences de Bizerte, Université de Carthage, Zarzouna 7021, Tunisia.

E-mail addresses: inoubliabdelwaheb@yahoo.fr, inoubli.abdelwaheb@gmail.com (A. Inoubli).

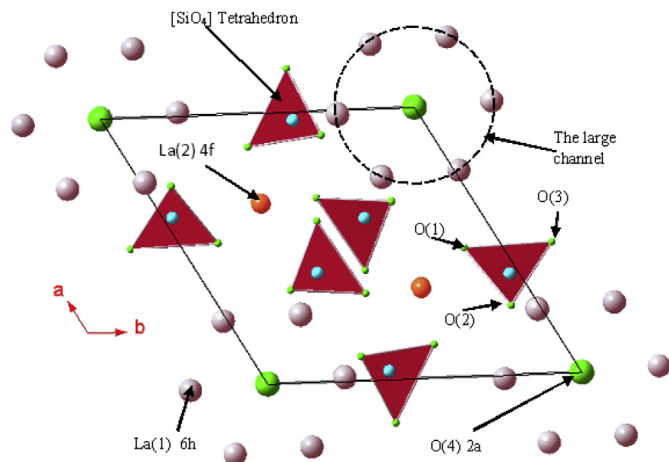


Fig. 1. Structure of the oxyapatite-type compound, $\text{La}_{9.33}\text{Si}_6\text{O}_{26}$ showing SiO_4 tetrahedrons and La–O channels.

example, Yoshioka et al. [14] found that the conductivity of oxyapatite-type $\text{La}_{10}\text{Si}_6\text{O}_{27}$ compounds is enhanced by the doping of Mg^{2+} . In addition, doping trivalent cations such as Al^{3+} and Ga^{3+} for the Si^{4+} site has also a positive effect on conductivity [15,16]. Recently, aluminum-doped lanthanum silicates with Al doping onto the Si site have attracted much attention due to their better properties [17–20]. However, the influence of the different Al doping amounts on $\text{La}_{9.33}\text{Si}_6\text{O}_{26}$ has seldom been systematically studied. In order to complete the lanthanum silicates system, a series of oxyapatite-type $\text{La}_{9.33}\text{Si}_{6-x}\text{Al}_x\text{O}_{26-x/2}\text{P}_{x/2}$ ($x = 0, 0.4, 0.8$ and 1) compounds, synthesized by the solid state reaction method [10,12,21–23].

In this report, the crystal structure of lanthanum silicate was studied by XRD patterns. The MAS-NMR technique is very sensitive at the local level, thus allowing the differentiation of the different environments. A Rietveld analysis was carried out using the XRD patterns of the synchrotron radiation to refine the lattice parameter and the Al^{3+} occupation sites [24]. In this study an attempt has been made to control the mobility of oxygen O(4) ions. In all these samples the amount of cationic vacancies was maintained close to 0.67 per lattice unit. The relationship between the crystallographic parameters and the conductivities when performing the Al

substitution is reported here in order to discuss the mobility of the oxide ions within this structure.

2. Experimental

The series of $\text{La}_{9.33}\text{Si}_{6-x}\text{Al}_x\text{O}_{26-x/2}\text{P}_{x/2}$ ($x = 0, 0.4, 0.8$ and 1) compounds was synthesized via the high temperature solid state reaction using the lanthanum oxide La_2O_3 (Sigma–Aldrich, Purity = 99%), silicon SiO_2 (Sigma–Aldrich, Purity > 99%), and metakaolinite $\text{Si}_4\text{Al}_4\text{O}_{14}$, which was prepared by heating kaolinite $\text{Si}_4\text{Al}_4\text{O}_{10}(\text{OH})_8$ with a high purity (Caobar, Spain) at 850°C for 2 h in air as a secondary source of Si and Al. In order to attain complete decarbonation and dehydroxylation, precalcining of La_2O_3 powder was performed at 1000°C for 1 h before weighing.

The XRD patterns of the oxyapatite were measured with a Bruker D8 ADVANCE diffractometer using $\text{CuK}\alpha_1$ radiation ($\lambda_{\text{CuK}\alpha_1} = 1.5406 \text{ \AA}$). The total measurement time was approximately 7 h per pattern so as to have good statistics over the $10\text{--}110^\circ$ (2θ) angular range, with a 0.0197° step size. Rietveld refinements of the XRD patterns were performed using FULLPROF software [25]. The ^{29}Si and ^{27}Al MAS-NMR spectra were recorded using a Bruker MSL400 (9.4T) spectrometer operating at 79.49 MHz for ^{29}Si and 104.26 MHz for ^{27}Al .

Finally, the electrical measurements of real and imaginary components of the impedance parameters (Z' and Z) were made over a wide range of temperatures ($400\text{--}750^\circ\text{C}$), with a cooling rate of 5°C min^{-1} and a stabilization time of 10 min between consecutive measurements and a frequency of (10 Hz–13 MHz), by means of a Hewlett Packard HP 4192A impedance analyzer. The pellet samples were obtained by applying 6500 kg cm^{-2} of pressure, followed by sintering at 1450°C for 2 h. Electrodes were made by coating opposite faces of the pellets with conductive silver paint and firing them at 450°C to eliminate the organic components and harden the Ag residue.

3. Results and discussion

3.1. XRD results

The XRD patterns of the kaolinite and metakaolinite (kaolinite heating at 850°C) are shown in Fig. 2. The kaolinite is identified by its first reflection at 12° (2θ). Metakaolinite is an almost pure kaolinite material, with the presence of an amount of quartz (SiO_2)

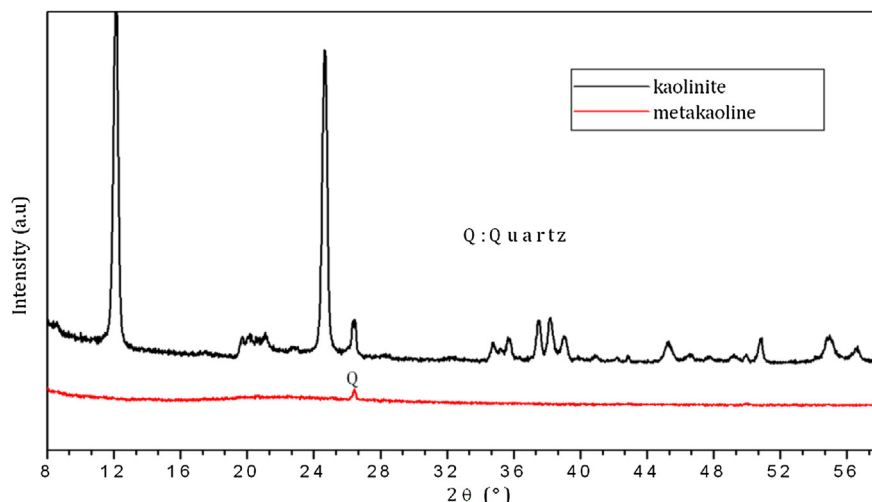


Fig. 2. XRD patterns of kaolinite and metakaolinite (kaolinite calcinated in air at 850°C).

which is identified by a peak at around 26° (2θ) [26,27]. When kaolinite loses structural water, the peaks disappeared indicating the appearance of metakaolinite, its XRD pattern becomes characteristic of an amorphous phase (metakaolinite) [26–29], constituted of lamellar particles. XRD patterns of the analyzed samples of $\text{La}_{9.33}\text{Si}_{6-x}\text{Al}_x\text{O}_{26-x/2}\text{P}_{x/2}$ ($x = 0, 0.4, 0.8$ and 1) are given in Fig. 3. All samples exhibited sharp diffraction peaks indicative of well-crystallized phases. The main phase was oxyapatite with a very small amount of the lanthanum silicate $\text{La}_2\text{Si}_2\text{O}_7$ as a secondary phase, for $x = 0$. Peak positions were in good agreement with the JCPDS file No. 01-074-2986 of the $\text{La}_{9.33}\text{Si}_6\text{O}_{26}$ phase (Space Group P-3 (No. 147)). The sample symmetry used for the refinement was P63/m (No. 176).

The structural study using the Rietveld technique is shown in Fig. 4, it shows a good agreement (blue line) between the experimental (red star) and calculated diagrams (black star). The refined atomic positions of the $\text{La}_{9.33}(\text{SiO}_4)_6\text{O}_2$ compound are similar to those proposed by Léon-Reina [8], Masubuchi [10], Okudera [13] and Iwata [30]. As shown in Fig. 1, the oxide ions occupy four different sites, three of which are located close to the Si site (O(1) (6h), O(2) (6h), O(3) (12i) with one oxide-ion site located at the corner of the unit cell (O(4) (2a)). Refinement of the relative site occupancies suggested values of 0.83 and 0.17 for La (2) and the vacancy respectively. Final Rietveld refinements showed good figures of merit with a goodness of fit (χ^2) ranging between 3.47 and 5.38. Refined unit cell parameters, occupations and the atomic positions are given in Table 1. Lanthanides La (1) and La (2) were distributed along the 6h and 4f sites respectively and the O (4) anion along the 2a site. The occupancies were initially taken in order to refine the sub-stoichiometric oxygen composition where the La (1) cations are completely occupied. Indeed, cationic vacancies of these four oxyapatite compounds are preferably located in the La(2) (4f) site. The occupancy rate of Si ranges from 1 ($x = 0$) to 0.83 ($x = 1$) and that of Al ranges from 0 ($x = 0$) to 0.17 ($x = 1$), this difference is related to the aluminum that was chosen to substitute the 6h site of Si in the $\text{La}_{9.33}\text{Si}_{6-x}\text{Al}_x\text{O}_{26-x/2}\text{P}_{x/2}$ ($x = 0.4, 0.8$ and 1) compounds. The O(4) site, located in large conduction channels, has an occupancy rate which varies according to the stoichiometry of the oxyapatite and which is equal to 0.9 for $x = 0.4$, 0.8 for $x = 0.8$ and 0.75 for $x = 1$. Anionic vacancies of the compounds for sub-stoichiometric oxygen are located in the O(4) sites.

The oxyapatite compounds studied in this paper are built from isolated $[\text{TO}_4]$ tetrahedrons (where T is Si or Al) with a mean T–O distance of 1.618 Å and a mean O–T–O angle of 109.36° (Table 2).

Whereas the average values for the O–T–O angles for all samples are very close to the ideal value of 109.36° , individual O–T–O angles range from 100.2° to 119° . The spread in the individual T–O distances and O–T–O angles is small, corresponding to an essentially regular tetrahedral coordination. The La cations are distributed among two crystallographically different positions. La(1) (6h Wyckoff site) is bound to seven oxygen atoms, whereas La(2) (4f Wyckoff site) has nine close oxygen neighbors up to 3.028 Å away. The bond lengths between the 6h site and said oxygen atoms range from 2.306 (6h–O(4)), for $x = 0.4$, to 2.315 Å (6h–O(1)) for $x = 1$. The O(4) atoms, or free oxygen, aren't linked to any of them (La(1) and La(2)), but the La(1)–O(4) distance built the large conduction channel.

3.2. ^{29}Si and Al MAS NMR spectroscopic study

For a better understanding of the process for the formation of the oxyapatite structure, ^{29}Si and ^{27}Al MAS NMR spectroscopy was used (Figs. 5 and 6), where the substitution of Si^{4+} by Al^{3+} was made with the aim to increase the amount of anionic vacancies (cannot avoid some Al in the La). The ^{29}Si MAS-NMR spectra of Al-doped oxyapatite samples exhibit four peaks at approximately -77.6 , -79.4 , -81.3 and -85.5 ppm and which were attributed to the different environments of silicon (Fig. 5). Four peaks were present for sample $x = 0$ devoid of Al, two peaks for $x = 0.4$ and 0.8 , and only one peak for the sample with a very large amount of Al or with large amounts of anionic vacancies ($x = 1$). Two overlapping peaks at -77.6 and -79.4 ppm corresponding to $[\text{SiO}_4]$ tetrahedrons of the Q^0 type, while those at -81.3 and -85.5 ppm seem to be due to $[\text{SiO}_4]$ tetrahedrons of Q^1 type [31–34]. The same features for apatite-type silicates were reported by Sansom et al., who suggest that they correspond to local distortions caused by the presence of cationic vacancies and interstitial oxide ion defects [33]. Especially in the case of sample $x = 0$, the main peak is slightly shifted to the left, may be due to the presence of an additional peak detected in the XRD patterns and that corresponds to the $\text{La}_2\text{Si}_2\text{O}_7$ secondary phase. The ^{29}Si MAS NMR spectra show a signal at -77.6 ($x = 0$) or -78.1 ppm ($x = 0.4, 0.8$ and 1), which characterizes the oxyapatite phase, which agrees with the XRD patterns. The ^{27}Al NMR spectra (Fig. 6) for all samples contain one intense peak at 76.72 ppm, characteristic of Al in tetrahedral coordination $[\text{AlO}_4]$ and another much less intense located at 11.6 ppm, corresponding to octahedral $[\text{AlO}_6]$ units. This observation is in agreement with the suggested substitution of silicon by Al.

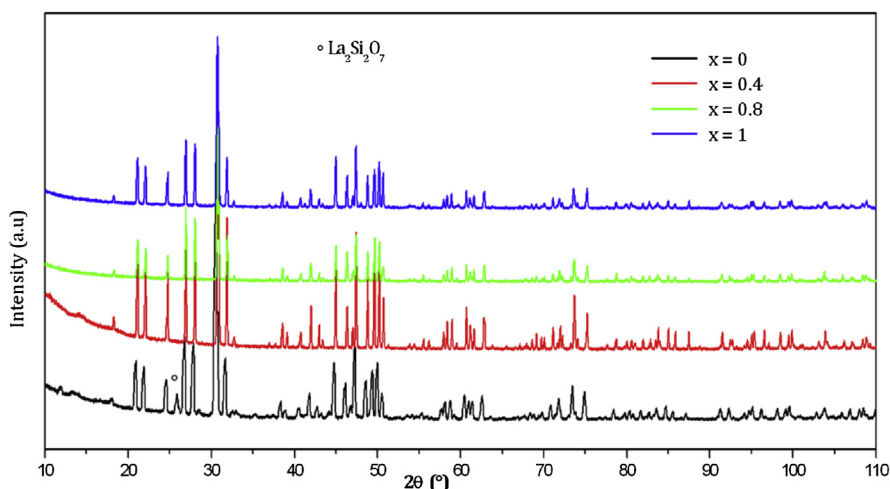


Fig. 3. XRD patterns of $\text{La}_{9.33}\text{Si}_{6-x}\text{Al}_x\text{O}_{26-x/2}\text{P}_{x/2}$ ($x = 0, 0.4, 0.8$ and 1).

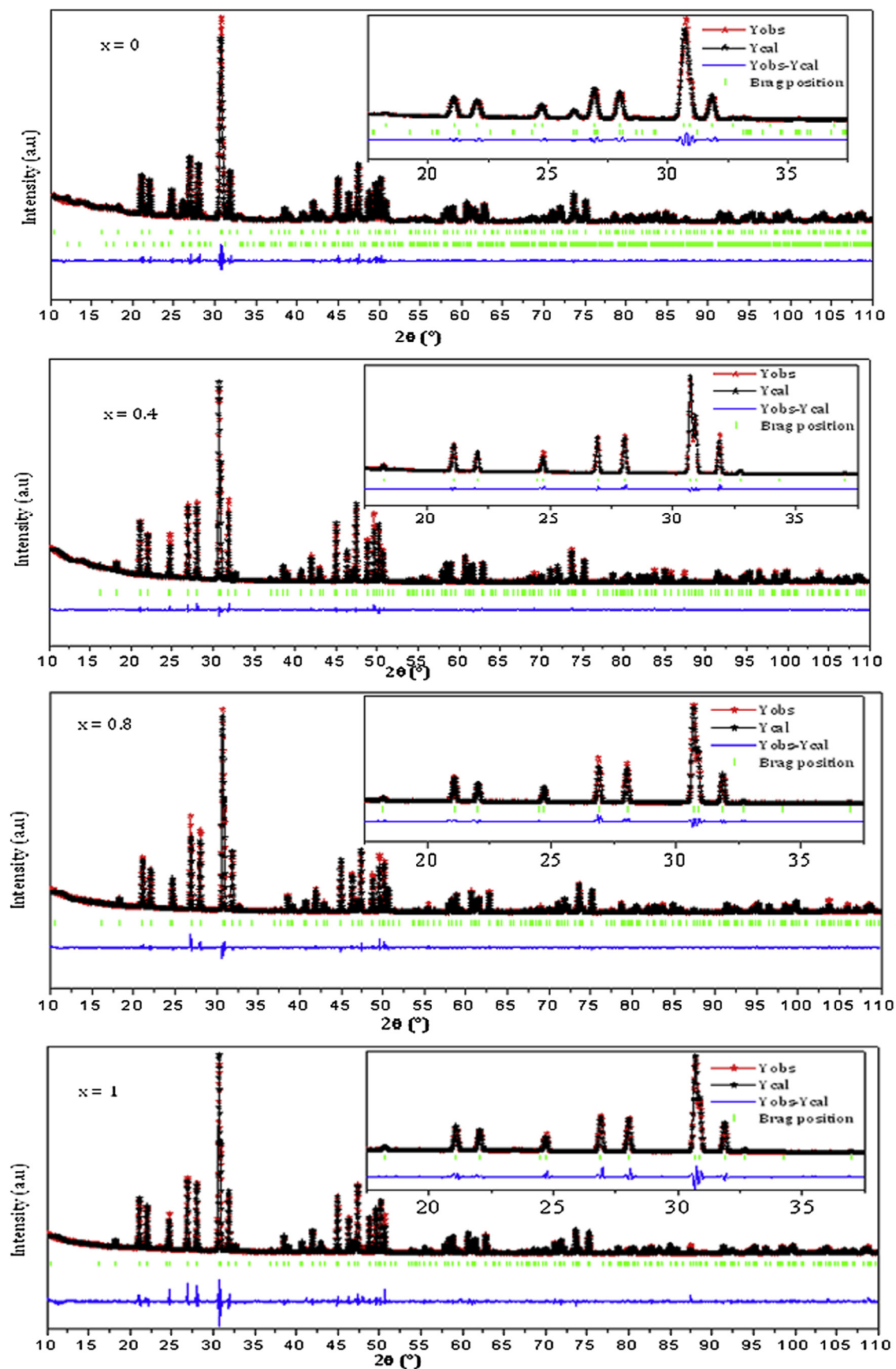


Fig. 4. Rietveld plot of $\text{La}_{9.33}\text{Si}_{6-x}\text{Al}_x\text{O}_{26-x/2}\text{O}_{x/2}$ ($x = 0, 0.4, 0.8$ and 1), experimental (red star), calculated (black star) and difference (blue line). (For interpretation of the references to colour in this figure legend, the reader is referred to the web version of this article.)

Table 1Cell and atomic parameters of $\text{La}_{9.33}\text{Si}_6-x\text{Al}_x\text{O}_{26-x/2}\text{O}_{x/2}$ ($x = 0, 0.4, 0.8$ and 1).

x	0	0.4	0.8	1
$a(\text{\AA})$	9.7271	9.7159	9.7193	9.7186
$c(\text{\AA})$	7.1917	7.1949	7.2048	7.2045
La(1), $(x,y,0.25)$				
x	0.0132	0.0140	0.0148	0.0131
y	0.2444	0.2441	0.2447	0.2445
La(2),4f, (0.33, 0.66, z)				
z	0.0034	0.0048	0.0037	0.0023
Occupancy	0.83	0.83	0.83	0.83
(Si/Al),6h, $(x,y,0.25)$				
x	0.4040	0.4042	0.4036	0.4015
y	0.3701	0.3762	0.3681	0.3676
Occupancy	1	0.93/0.07	0.87/0.13	0.83/0.17
O(1),6h, $(x,y,0.25)$				
x	0.3302	0.3202	0.3330	0.3206
y	0.4870	0.4710	0.4880	0.4901
O(2),6h, $(x,y,0.25)$				
x	0.5347	0.5242	0.5310	0.5278
y	0.1280	0.1330	0.1260	0.1270
O(3),12i, (x,y,z)				
x	0.3496	0.3265	0.3448	0.3401
y	0.2545	0.2512	0.2630	0.2515
z	0.0702	0.0734	0.0816	0.0665
O(4),2a,(0,0,0.25)				
Occupancy	1	0.9	0.8	0.75
R_B	3.09	6.33	5.93	4.95
R_F	2.17	5.09	4.2	4.78
Goodness of fit	5.38	5	3.47	3.54

The peak at 76.7 ppm may be related to the incorporation of Al into Si sites in the formed apatite. The ^{29}Si MAS-NMR study of the samples showed the presence of a main component which was detected at -78 ppm, shifted for sample $x = 0$ and which could be due to the presence of a secondary phase. The ^{27}Al MAS-NMR study of the samples showed the existence of Al in the tetrahedral site by

Table 2Interatomic distance (\AA) and angles ($^\circ$) of $\text{La}_{9.33}\text{Si}_6-x\text{Al}_x\text{O}_{26-x/2}\text{O}_{x/2}$ ($x = 0, 0.4, 0.8$ and 1).

x	0	0.4	0.8	1
La(1) (6h)				
La–O(1)	2.7916	2.6730	2.8006	2.7377
La–O(2)	2.5786	2.4729	2.5362	2.4959
La–O(3)($\times 2$)	2.4497	2.4358	2.5387	2.4330
La–O(3)($\times 2$)	2.6128	2.5918	2.6446	2.6000
La–O(4)	2.3158	2.3067	2.3098	2.3152
Mean	2.5444	2.5011	2.5733	2.5164
La(2) (4f)				
La–O(1)($\times 3$)	2.5139	2.5972	2.5201	2.4600
La–O(2)($\times 3$)	2.4912	2.4747	2.5082	2.5141
La–O(3)($\times 3$)	2.9162	3.0285	2.9035	2.8975
Mean	2.6404	2.7001	2.6439	2.6238
T (Si/Al)(6h)				
T–O(1)	1.6216	1.5070	1.6213	1.7238
T–O(2)	1.5753	1.7234	1.6118	1.6649
T–O(3)($\times 2$)	1.6191	1.6561	1.5028	1.6443
Mean	1.6087	1.6356	1.5596	1.6693
Angles				
O(1)–T–O(2)	113.2	119	109.8	111.3
O(1)–T–O(3)	109.4	105.1	109.5	109.9
O(2)–T–O(3)	109.6	112.8	110.1	109.3
O(3)–T–O(3)	106.0	100.2	107.6	107.0
Mean	109.55	109.28	109.25	109.37

the presence of a component at 76.7 ppm. This observation is in agreement with the suggested substitution of Al^{3+} into the Si^{4+} site.

3.3. Ionic conductivity

Fig. 7 shows the complex impedance plots ($-Z'$ vs Z'') of the $\text{La}_{9.33}\text{Si}_6\text{O}_{26}$ sample pellet sintered at 1450°C and its corresponding equivalent circuit used to obtain the resistance and capacitance of each contribution. The equivalent circuits consisted of a serial association of ($R//\text{CPE}$) elements attributed to electrolyte or electrode processes: Grain resistance (R_1), grain boundary resistance (R_2), grain capacitance (CPE_1) and grain boundary capacitance (CPE_2), where R is resistance and CPE is a Constant Phase Element. The impedance curves consist of a semicircle shifted from the origin, and not centered on the real axis. When the temperature increases, the semicircle associated with the relaxation phenomena due to the bulk at high frequency almost disappears. It is difficult to separate the contributions between 400 and 450°C associated with the bulk and grain boundary respectively at high and intermediate frequency. Only a semicircle is observed, which corresponds to the total resistance of the material. The relaxation frequencies of the bulk and the grain boundary are very close, which explains the overlap of the two contributions. The impedance response of this oxyapatite consists of two semicircles: One semicircle at high frequency (2×10^5 – 13×10^6 Hz) attributable to the bulk (b), and another one appearing at an intermediate frequency (10 – 2×10^5 Hz), corresponding to the grain boundary (gb). The contribution at a low frequency of under 10^2 Hz (response of the electrode interface), is not fully observed in this case. As shown in Fig. 7, for the impedance curves from 650°C , the grain boundary resistance increases visibly with the increase in temperature; this suggests considerable grain boundary contribution to the total resistance of the oxyapatite electrolyte at high temperatures. Fig. 8 shows the variation in the conductivity of the bulk and grain boundary in a temperature range of 550 – 700°C . For this sample, and temperatures 650 and 700°C , the bulk conductivity is higher than that of the grain boundary. At 700°C , there is a difference of a factor of about 2.5 between the measured conductivity of the bulk ($\sigma_b = 1.8 \times 10^{-3} \text{ S cm}^{-1}$) and the grain boundary ($\sigma_{gb} = 7.2 \times 10^{-4} \text{ S cm}^{-1}$). In addition, the activation energy of the bulk ($E_{ab} = 1.5 \text{ eV}$) is higher than that of the grain boundary ($E_{agb} = 0.86 \text{ eV}$). Thus, the conductivity of the oxyapatite appears limited by the conductivity of the grain boundary. From 700°C , only a contribution of the electrodes is observed for sample $x = 1$ (Fig. 9).

Fig. 9 shows the impedance plots of the $\text{La}_{9.33}\text{Si}_6-x\text{Al}_x\text{O}_{26-x/2}\text{O}_{x/2}$ ($x = 0.4, 0.8$ and 1) samples at different temperatures. The impedance spectra in the 400 – 750°C temperature range for $x = 0.4$ and $x = 0.8$ consist of two semicircles, one at high frequency due to the bulk and another one at an intermediate frequency attributable to the grain boundary. For $x = 1$, and in the 450 – 600°C temperature range, the impedance spectra consists of three semicircles, one semicircle attributed to the bulk response followed by a second one attributed to the grain boundary response, and a third one at low frequency attributed to the electrode interface. The impedance spectra registered between 550 and 750°C appears as an inductive contribution at high frequency. However, at different temperatures, the ($x = 1$) sample has semicircles which are smaller than for other samples, which shows the enhancing conductivity. The enhancement of the conductivity is based on the substitution of lower valence cations such as Al^{3+} .

Indeed, Abram et al. [35] have explained the improvement of the conductivity as a function of the Al^{3+} doping by the optimization of the number of vacancies in the La site. However, the authors of Ref. [36] underlined a significant reduction of the positive charge

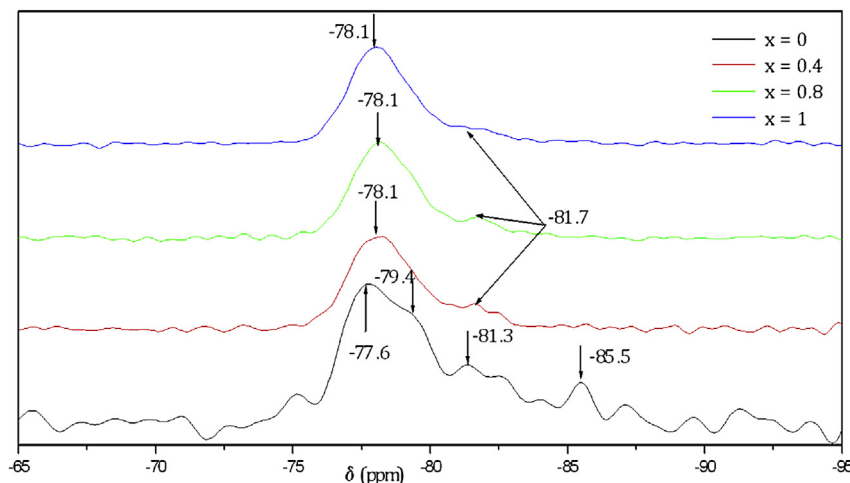


Fig. 5. ^{29}Si NMR MAS spectra of $\text{La}_{9.33}\text{Si}_{6-x}\text{Al}_x\text{O}_{26-x/2}\square_{x/2}$ ($x = 0, 0.4, 0.8$ and 1).

on the tetrahedron site that may affect the local distortion of SiO_4 tetrahedrons and thus have a large effect on the migration of oxide ions. The conductivity of the material is the inverse of the sum of the bulk resistance and the grain boundary resistance. The total resistance is obtained as the resistance value at the intercept with the real axis. The conductivity data for the oxyapatite can be converted from the total resistance data, R , through the following equation:

$$\sigma = \frac{e}{S \cdot R}$$

where e is the sample thickness, S is the pellet surface area and R is the total resistance.

When the conductivity values for undoped oxyapatite ($x = 0$) were compared with those in the literature (between $\sigma = 3 \times 10^{-3}$ to $1.1 \times 10^{-4} \text{ S cm}^{-1}$) at 700°C according to [6,7,15,37,38], the results were found to be consistent with what has been reported in the literature ($\sigma = 7.4 \times 10^{-4} \text{ S cm}^{-1}$) at 700°C . However, migration of oxide ions is an interstitial mechanism [39]. The presence of cationic vacancies (0.67) promotes the relaxation of SiO_4

tetrahedrons to this empty position lanthanum, and oxygen migration is favored in the doped samples [39].

Fig. 10 shows the Arrhenius plots of $\ln(\sigma T)$ vs $1000/T$ for the conductivity of the different samples at different temperatures. Identical slopes are observed for these samples ($x = 0.4, 0.8$ and 1), which results in similar activation energies (E_a is between 0.946 and 0.8 eV), confirming the same mechanism of conduction. The activation energy does not change linearly with the doped aluminum content. For oxyapatites, Islam et al. [40] showed that a vacancy mechanism is characterized by a high activation energy ($>1.1 \text{ eV}$), while the migration of the interstitial oxygen is linked to a lower activation energy, near 0.7 eV [7,38,41]. The conductivity of oxyapatite compounds increases with the doped aluminum content in the structure. However, when trivalent Al^{3+} is substituted for tetravalent Si^{4+} , more oxygen vacancies are generated in order to keep a charge balance of the crystal structure, and in this case the carriers contain both cationic and oxygen vacancies collectively, which consequently improves the conductivity. As can be seen from Fig. 11 conductivity and the $\text{La}(1)\text{--O}(4)$ distances increase by increasing the Al content. This indicates that the conduction is provided by the increase in the $\text{La}(1)\text{--O}(4)$ distance, facilitating the

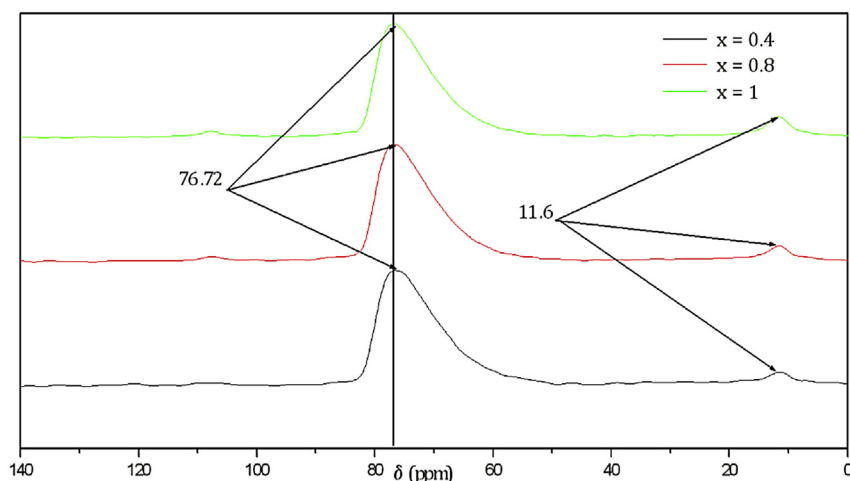


Fig. 6. ^{27}Al NMR MAS spectra of $\text{La}_{9.33}\text{Si}_{6-x}\text{Al}_x\text{O}_{26-x/2}\square_{x/2}$ ($x = 0.4, 0.8$ and 1).

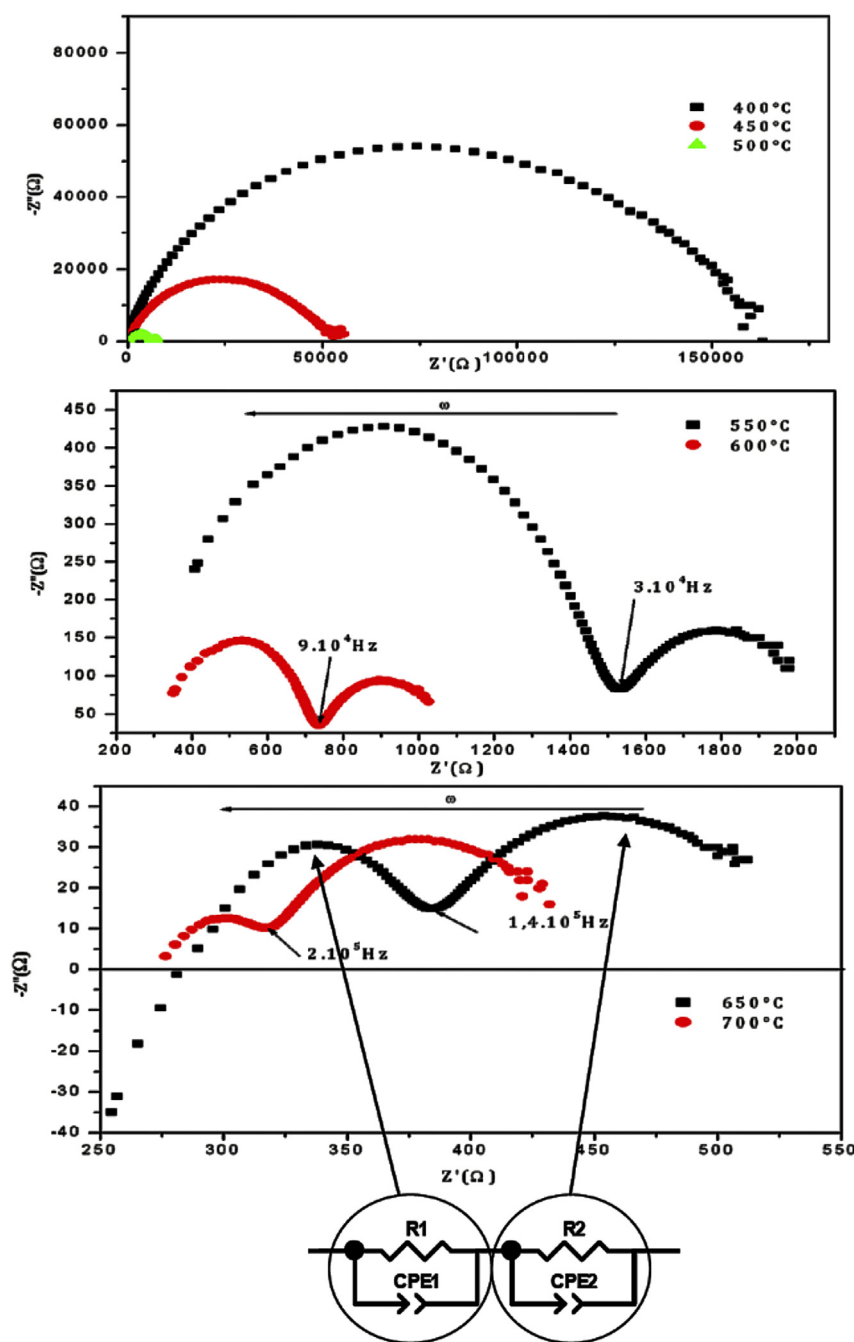


Fig. 7. Impedance plots and corresponding equivalent circuit of $\text{La}_{0.33}\text{Si}_6\text{O}_{26}$.

O^{2-} ion migration and thus enhancing the conduction. The conductivity decreases from the sample where $x = 0$ to the sample where $x = 0.4$, as this distance decreases very rapidly. This can be explained by a possible change in the conduction mechanism which is confirmed by the decrease of the activation energy (from 1.4 to 0.93 eV). The insertion of the aluminum structure, extends this distance and improves the conductivity from $x = 0.4$ to $x = 1$. The presence of some oxygen vacancies seems to be favorable to the conduction. However, the undoped oxyapatite ($x = 0$) ($\sigma = 7.4 \times 10^{-4} \text{ S cm}^{-1}$ at 700 °C) shows a significant conductivity despite the absence of oxygen vacancies. The creation of a limited number of anionic vacancies ($x = 0.4, 0.8$ and 1) improves the conductivity with a slight variation of the activation energy (in the

order of 0.1 eV). The appearance of oxygen vacancies therefore facilitates the diffusion of oxygen through the structure. The creation of oxygen vacancies in the channels should probably change the profile of the diffusion pathways. It is not easy to correlate the dimensions of the conduction channels in lattice parameters, but it can be assumed that the best conductivity (for $x = 1$ aluminum atoms per unit cell) is due to an expansion of the channels ($\text{La}(1) - \text{O}(4)$ distance). The best conductivities attained were 2.75×10^{-3} and $5 \times 10^{-3} \text{ S cm}^{-1}$ at 700 and 750 °C respectively for $x = 1$, compared with the literature [39,42,43], which is lower than reported for yttria stabilized zirconia (YSZ) electrolyte [40] (Table 3). The favored electrolyte is YSZ, which exhibits a good oxide ion conductor at high temperatures.

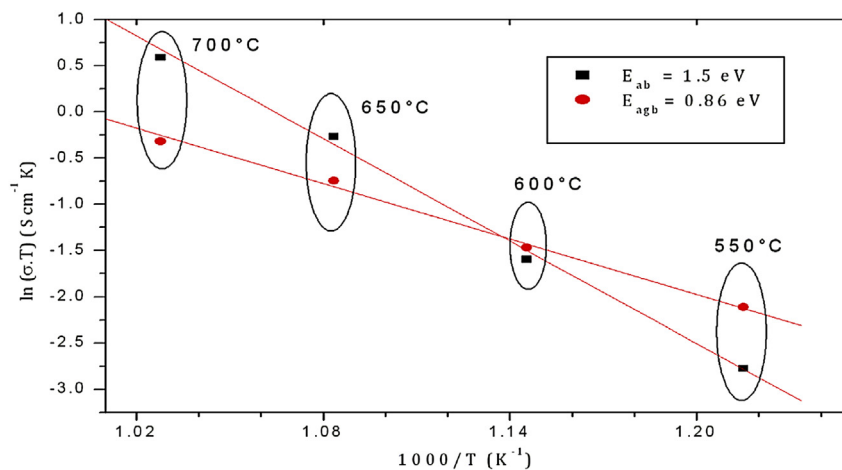


Fig. 8. Impedance plots at different temperatures of $\text{La}_{9.33}\text{Si}_{6-x}\text{Al}_x\text{O}_{26-x/2}\square_{x/2}$ ($x = 0.4, 0.8$ and 1).

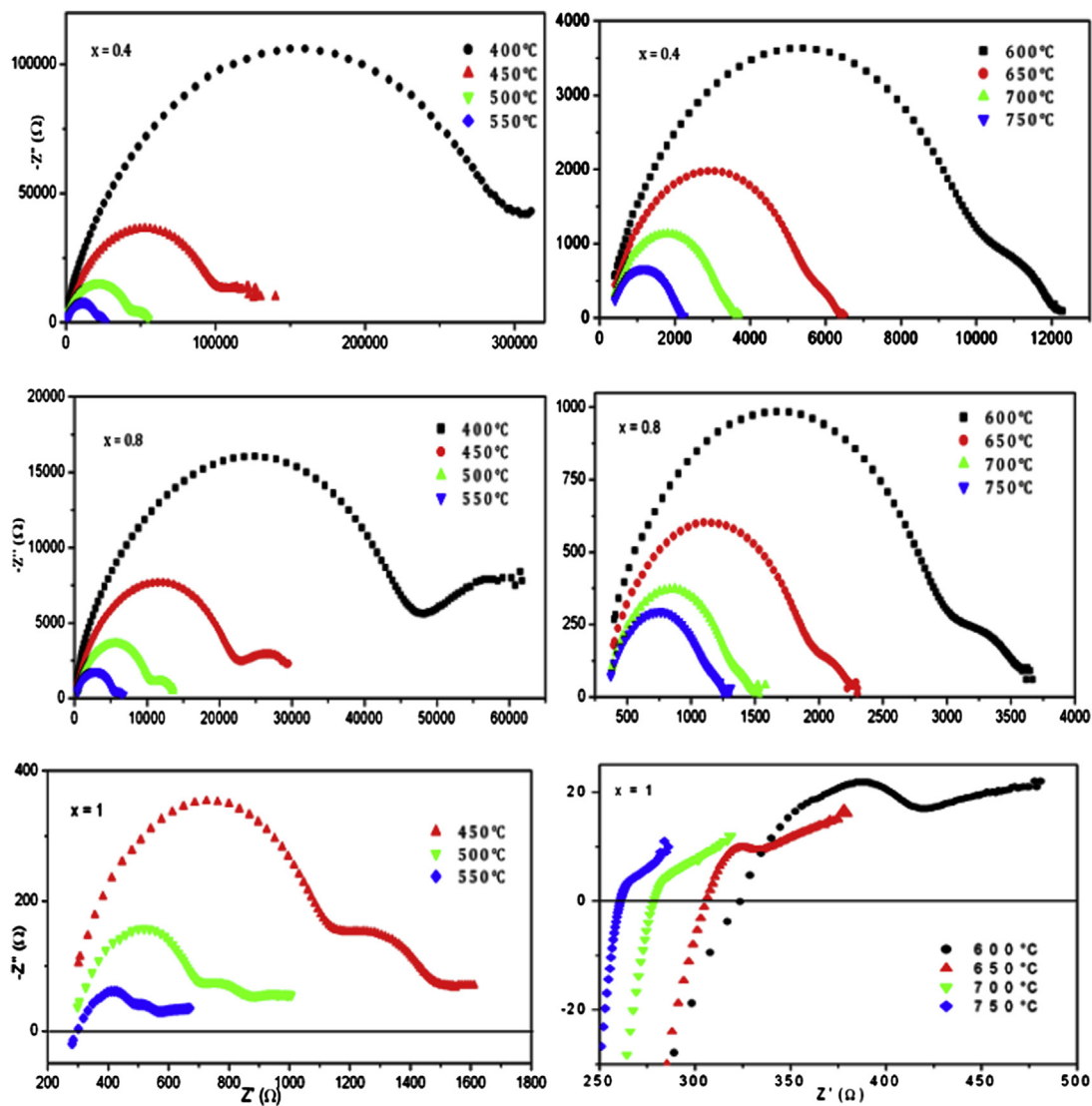


Fig. 9. Arrhenius plots of conductivity of $\text{La}_{9.33}\text{Si}_{6-x}\text{Al}_x\text{O}_{26-x/2}\square_{x/2}$ ($x = 0.4, 0.8$ and 1).

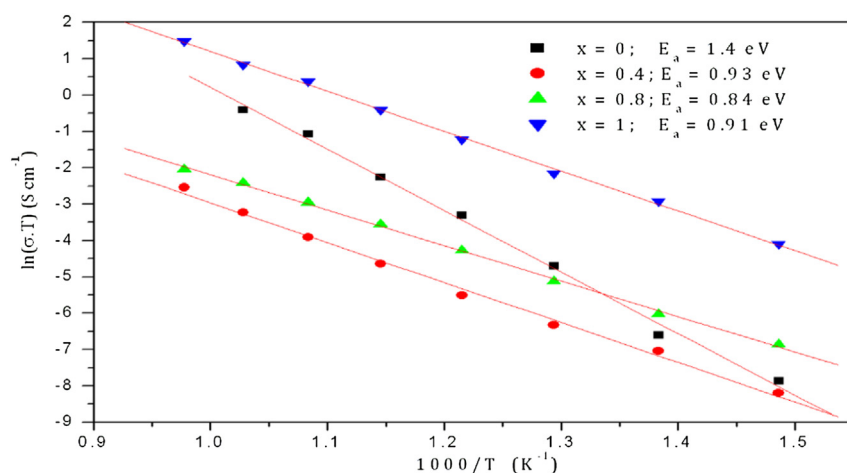


Fig. 10. Temperature dependence of bulk and grain boundary conductivity of $\text{La}_{9.33}\text{Si}_6\text{O}_{26}$.

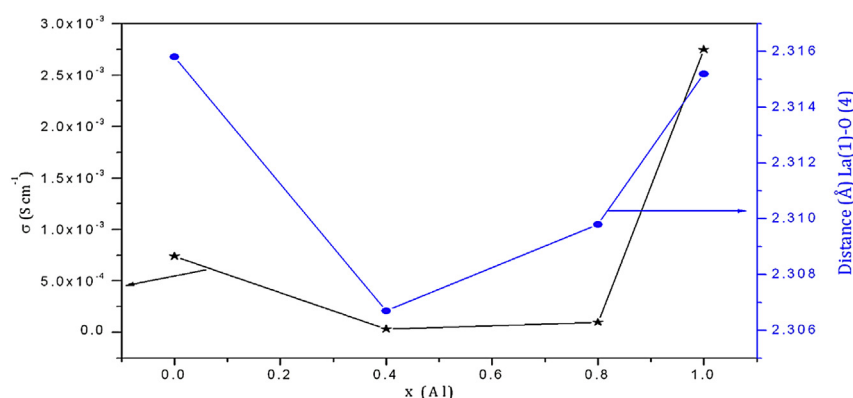


Fig. 11. Plots of the conductivity at 700 °C and La(1)–O(4) distance with Al content.

4. Conclusion

Substituted oxide conductors with the formula $\text{La}_{9.33}\text{Si}_{6-x}\text{Al}_x\text{O}_{26-x/2}\text{O}_{x/2}$ have been prepared by solid reaction synthesis at high temperature. The aim was to create oxide ion vacancies and to study their influence on the electrical properties of the material. Structural features of the oxyapatite ($\text{La}_{9.33}\text{Si}_{6-x}\text{Al}_x\text{O}_{26-x/2}\text{O}_{x/2}$) series have been deduced by the Rietveld analysis of XRD patterns. The conductivity for Al-doped oxyapatites and the La(1)–O(4) distances increased with the Al content

increase in the structure. The conducting channels must be large enough to allow the diffusion of the oxide ions. Lanthanum silicates doped with trivalent Al^{3+} have a higher conductivity than undoped $\text{La}_{9.33}\text{Si}_6\text{O}_{26}$. At 750 °C, sample $x = 1$ has the highest conductivity ($5 \times 10^{-3} \text{ S cm}^{-1}$), which is considerably higher than that of undoped $\text{La}_{9.33}\text{Si}_6\text{O}_{26}$. This compound is therefore a candidate to be used as an electrolyte in solid oxide fuel cells at high temperatures.

Acknowledgments

This work was supported by Spanish Agency of International Cooperation (AECI-B/026856/09). The authors are also grateful to ICMM for the RMN-MAS analysis and would like to thank the language expert Nayua Abdelkefi for proofreading the manuscript.

References

- [1] S.M. Hosseini, T. Shvareva, A. Navrotsky, *Solid State Ionics* 233 (2013) 62–66.
- [2] M. Santos, C. Alves, F.A.C. Oliveira, T. Marcelo, J. Mascarenhas, A. Cavaleiro, B. Trindade, *J. Power Sources* 231 (2013) 146–152.
- [3] A. Orera, T. Baikie, E. Kendrick, J.F. Shin, S. Pramana, R. Smith, T.J. White, M.L. Sanjuan, P.R. Slater, *Dalton Trans.* 40 (2011) 3903–3908.
- [4] F. Sun, N.N. Zhang, J.L. Li, H.L. Liao, *J. Power Sources* 223 (2013) 36–41.
- [5] S. Nakayama, A. Ikesue, Y. Higuchi, M. Sugawara, M. Sakamoto, *J. Eur. Ceram. Soc.* 33 (2013) 207–210.
- [6] J.E.H. Samson, J.R. Tolchard, P.R. Slater, M.S. Islam, *Solid State Ionics* 167 (2004) 17–22.
- [7] J.E.H. Sansom, D. Richings, P.R. Slater, *Solid State Ionics* 139 (2001) 205–210.

Table 3

Conductivity values reported in the literature.

Compounds	Conductivity (S cm^{-1}) at 700 °C	Ref.
$\text{La}_{10}\text{Si}_5\text{AlO}_{26.5}$	1.95×10^{-3} sintered at 1500 °C	[39]
	1.55×10^{-3} sintered at 1450 °C	
$\text{La}_{9.83}\text{Si}_{4.5}\text{Al}_{1.5}\text{O}_{26}$	7.9×10^{-4} sintered at 1500 °C	[39]
$\text{La}_{9.83}\text{Si}_5\text{AlO}_{26.25}$	9.9×10^{-4} sintered at 1500 °C	[42]
$\text{La}_{10}\text{Si}_5\text{AlO}_{26.5}$	1.2×10^{-3} sintered at 1470 °C	[42]
$\text{La}_{9.67}\text{Si}_6\text{O}_{26}$	0.9×10^{-4} sintered at 1470 °C	[42]
$\text{La}_{9.33}\text{Si}_5\text{AlO}_{25.5}$	2.75×10^{-3} sintered at 1450 °C	This work
$\text{La}_{10}\text{Si}_{5.5}\text{Al}_{0.5}\text{O}_{26.75}$	4.6×10^{-3} (800 °C) sintered at 1400 °C	[43]
$\text{La}_{9.83}\text{Si}_{5.5}\text{Al}_{0.5}\text{O}_{26.5}$	5.2×10^{-4} sintered at 1500 °C	[42]
$\text{Zr}_{0.85}\text{Y}_{0.15}\text{O}_{1.93}$ (8YSZ)	6.2×10^{-3} at 600 °C and 5.0×10^{-2} at 800 °C	[44]
$\text{La}_{9.42}\text{Si}_{5.75}\text{Al}_{0.25}\text{O}_{26}$	1.6×10^{-4} sintered at 1470 °C	[42]

- [8] L. Leon-Reina, E.R. Losolla, M. Marthinez-Lara, S. Bruque, M.A.G. Aranda, *J. Mater. Chem.* 14 (2004) 1142–1149.
- [9] L. Leon-Reina, M.C. Martin-Sedeno, E.R. Losilla, A. Cabeza, M. Martinez-Lara, S. Brusque, F.M.B. Marques, D.V. Sheptyakov, M.A.G. Aranda, *Chem. Mater.* 15 (2003) 2099–2108.
- [10] Y. Masubuchi, M. Higuchi, T. Takeda, S. Kikkawa, *Solid State Ionics* 177 (2006) 263–268.
- [11] S. Guillot, S. Beaudet-Savignat, S. Lambert, R.N. Vannier, P. Roussel, F. Porcher, *J. Solid State Chem.* 182 (2009) 3358–3364.
- [12] S. Beaudet-Savignat, A. Vincent, S. Lambert, F. Gervais, *J. Mater. Chem.* 17 (2007) 2078–2087.
- [13] H. Okudera, Y. Masubuchi, S. Kikkawa, A. Yoshiasa, *Solid State Ionics* 176 (2005) 1473–1478.
- [14] H. Yoshioka, S. Tanase, *Solid State Ionics* 176 (2005) 2395–2398.
- [15] S. Chefi, A. Madani, H. Boussetta, C. Roux, A. Hammou, *J. Power Sources* 177 (2008) 464–469.
- [16] E. Kendrick, P.R. Slater, *Mater. Res. Bull.* 43 (2008) 3627–3632.
- [17] A.L. Shaula, V.V. Kharton, F.M.B. Marques, *J. Solid State Chem.* 178 (2005) 2050–2061.
- [18] J. Zhou, X.F. Ye, J.L. Li, S.R. Wang, T.L. Wen, *Solid State Ionics* 201 (2011) 81–86.
- [19] G. Lucazeau, N. Sergent, T. Pagnier, A. Shaula, V. Kharton, F.M.B. Marques, *J. Raman Spectrosc.* 38 (2007) 21–33.
- [20] A. Mineshige, T. Nakao, Y. Ohnishi, M. Kobune, T. Yazawa, H. Yoshioka, *Electrochemistry* 77 (2009) 146–148.
- [21] A. Mineshige, T. Nakao, M. Kobune, T. Yazawa, H. Yoshioka, *Solid State Ionics* 179 (2008) 1009–1012.
- [22] W. Gao, H.L. Liao, C. Coddet, *J. Power Sources* 179 (2008) 739–744.
- [23] A. Brisse, A.L. Sauvet, C. Barthet, S. Georges, J. Fouletier, *Solid State Ionics* 178 (2007) 1337–1343.
- [24] L. León-Reina, J.M. Porras-Vázquez, E.R. Losilla, M.A.G. Aranda, *Solid State Ionics* 177 (2006) 1307–1315.
- [25] J. Rodríguez-Carvajal, *Phys. B Condens. Matter* 192 (1993) 55–69.
- [26] J. Sanz, A. Madani, J.M. Serratoza, *J. Am. Ceram. Soc.* 71 (1988) 418–421.
- [27] A. Madani, A. Aznar, J. Sanz, J.M. Serratos, *J. Phys. Chem.* 94 (1990) 760–765.
- [28] A.Á.B. Maia, R.S. Angélica, R. de Freitas Neves, H. Pöhlmann, C. Straub, K. Saalwächter, *Appl. Clay Sci.* 87 (2014) 189–196.
- [29] F. Zibouche, H. Kerdjoudj, J.-B. d'Espinose de Lacaillerie, H. Van Damme, *Appl. Clay Sci.* 43 (2009) 453–458.
- [30] T. Iwata, K. Fukuda, E. Béchade, O. Masson, I. Julien, E. Champion, P. Thomas, *Solid State Ionics* 178 (2007) 1523–1529.
- [31] R. Dupree, M.H. Lewis, M.E. Smith, *J. Am. Chem. Soc.* 111 (1989) 5125–5132.
- [32] T. Isobe, T. Watanabe, J.B. d'Espinose de la Caillerie, A.P. Legrand, D. Massiot, *J. Colloid Interface Sci.* 261 (2003) 320–324.
- [33] J.E.H. Sansom, J.R. Tolchard, M.S. Islam, D. Apperley, P.R. Slater, *J. Mater. Chem.* 16 (2006) 1410–1413.
- [34] T. Kharlamova, S. Pavlova, V. Sadykov, M. Chaikina, T. Krieger, O. Lapina, D. Khabibulin, A. Ishchenko, V. Zaikovskii, C. Argiris, J. Frade, *Eur. J. Inorg. Chem.* (2008) 939–947.
- [35] E.J. Abram, D.C. Sinclair, A.R. West, *J. Mater. Chem.* 11 (2001) 1978–1979.
- [36] A. Najib, J.E.H. Sansom, J.R. Tolchard, P.R. Slater, M.S. Islam, *Dalton Trans.* 19 (2004) 3106–3109.
- [37] A. Vincent, S. Beaudet Savignat, F. Gervais, *J. Eur. Ceram. Soc.* 27 (2007) 1187–1192.
- [38] P.R. Slater, J.E.H. Samson, *Solid State Phenom.* 90–91 (2003) 195–200.
- [39] X. Guo-Cao, S. Ping-Jiang, *J. Alloys Compd.* 523 (2012) 127–133.
- [40] M.S. Islam, J.R. Tolchard, P.R. Slater, *Chem. Commun.* (2003) 1486–1487.
- [41] S. Tao, J.T.S. Irvine, *Mater. Res. Bull.* 36 (2001) 1245–1258.
- [42] T. Kharlamova, S. Pavlova, V. Sadykov, O. Lapina, D. Khabibulin, T. Krieger, V. Zaikovskii, A. Ishchenko, A. Salanov, V. Muzykantov, N. Mezentseva, M. Chaikina, N. Uvarov, J. Frade, C. Argiris, *Solid State Ionics* 179 (2008) 1018–1023.
- [43] D. Marrero-López, L. dos Santos-Gómez, L. León-Reina, J. Canales-Vázquez, E.R. Losilla, *J. Power Sources* 245 (2014) 107–118.
- [44] N.H. Menzler, F. Tietz, S. Uhlenbruck, H.P. Buchkremer, D. Stöver, *J. Mater. Sci.* 45 (2010) 3109–3135.